ENGINEERING

Artificial visual systems enabled by quasi–two-dimensional electron gases in oxide superlattice nanowires

You Meng[1,2,3]*, Fangzhou Li[1]*, Changyong Lan[4], Xiuming Bu[1], Xiaolin Kang[1,2,3], Renjie Wei[1,2,3,5], SenPo Yip[1,2,3,5], Dapan Li[1,3], Fei Wang[1,2], Tsunaki Takahashi[6], Takuro Hosomi[6], Kazuki Nagashima[6], Takeshi Yanagida[6,7], Johnny C. Ho[1,2,3,5,7]†

Rapid development of artificial intelligence techniques ignites the emerging demand on accurate perception and understanding of optical signals from external environments via brain-like visual systems. Here, enabled by quasi–two-dimensional electron gases (quasi-2DEGs) in $InGaO_3(ZnO)_3$ superlattice nanowires (NWs), an artificial visual system was built to mimic the human ones. This system is based on an unreported device concept combining coexistence of oxygen adsorption-desorption kinetics on NW surface and strong carrier quantum-confinement effects in superlattice core, to resemble the biological Ca^{2+} ion flux and neurotransmitter release dynamics. Given outstanding mobility and sensitivity of superlattice NWs, an ultralow energy consumption down to subfemtojoule per synaptic event is realized in quasi-2DEG synapses, which rivals that of biological synapses and now available synapse-inspired electronics. A flexible quasi-2DEG artificial visual system is demonstrated to simultaneously perform high-performance light detection, brain-like information processing, nonvolatile charge retention, in situ multibit-level memory, orientation selectivity, and image memorizing.

INTRODUCTION

Human brain is one of the most complicated objects in our known universe. It consists of a massive collection of parallel and reconfigurable neural networks with gigantic numbers of neurons and neuronal junctions (synapses). These synapses can get strengthened or weakened over time in response to the increase or decrease in their activity. This ability of synapses is referred to as synaptic plasticity, where their event dependence constitutes the basis of parallel computing and distributed memory (*1*). Taking inspiration from the human brain, artificial neuromorphic systems that adopt an in-memory computing approach can address the energy and throughput inefficiency of conventional von Neumann computing architectures such that the data processing and memorizing units are no longer physically separated (*2*, *3*). In particular, owing to the dynamic changes of synaptic connection strength, the artificial synapses are capable to process data and identify patterns more robust, plastic, and fault tolerant, giving rise to the adaptivity to indeterministic information (*4*, *5*). All these exceptional characteristics of the neuromorphic computing architecture have made it of great interest for brain-inspired technological applications such as visual information processing, which involves enormous parallel data that are correlated.

Recently, fascinating quantized physical properties of complex oxide materials have been widely demonstrated with their strong carrier quantum-confinement effects (*6*, *7*). Representative examples include $LaAlO_3/SrTiO_3$ and MgZnO/ZnO heterointerfaces, where the superconductivity in $SrTiO_3$ (*8*) and the quantum Hall effect in ZnO-based heterostructures (*9*, *10*) are experimentally observed. After intensive investigations, it becomes clear that quasi–two-dimensional electron gases (quasi-2DEGs) formed at these heterointerfaces are the key to uncover these emergent phenomena. Strong electron correlations in these atomically abrupt oxide heterointerfaces can give rise to a rich variety of electronic phases, which makes these quasi-2DEGs highly susceptible to small changes of control parameters (e.g., electric field, magnetic field, or light irradiation) (*7*, *8*, *11*). Interactions between these quasi-2DEGs and control parameters would create advanced optoelectronic devices with tunable properties, e.g., nonvolatile resistive switching (*12*), ultrasensitive potentiometric biosensing (*13*), and giant persistent photoconductivity (PPC) (*14*). Given the high carrier mobility together with the high sensitivity to various stimuli, quasi-2DEG systems are anticipated to enable technological breakthroughs in the development of neuromorphic sensing systems, which can substantially lower energy consumption and enhance sensitivity that are not achievable by other material systems. Nevertheless, to the best of our knowledge, there are still no reports on the utilization of quasi-2DEGs for artificial neuromorphic systems.

At the same time, considering the ultrahigh surface-to-volume ratio of nanowires (NWs), their unique morphology would make them possible for massive probing of optical signals (*15*). To date, various NW technologies have been proven to have a number of advantages in terms of charge carrier transport, energy efficiency, mechanical flexibility, process scalability, and device miniaturization that usually outperform other counterparts. In this investigation, we propose an unreported device concept for quasi-2DEG photonic synapses based on the coexistence of oxygen adsorption-desorption kinetics on NW surfaces and strong carrier quantum-confinement effects in the superlattice core, to resemble the Ca^{2+} ion flux and neurotransmitter release dynamics in biological synapses. In particular, here, superlattice-structured $InGaO_3(ZnO)_3$ NWs are used to develop the quasi-2DEG–based artificial visual systems. The details of the

[1]Department of Materials Science and Engineering, City University of Hong Kong, Kowloon 999077, Hong Kong SAR. [2]State Key Laboratory of Terahertz and Millimeter Waves, City University of Hong Kong, Kowloon 999077, Hong Kong SAR. [3]Centre for Functional Photonics, City University of Hong Kong, Kowloon 999077, Hong Kong SAR. [4]School of Optoelectronic Science and Engineering, University of Electronic Science and Technology of China, Chengdu 610054, P. R. China. [5]Shenzhen Research Institute, City University of Hong Kong, Shenzhen 518057, P. R. China. [6]Department of Applied Chemistry, School of Engineering, University of Tokyo, Tokyo 113-8654, Japan. [7]Institute for Materials Chemistry and Engineering, Kyushu University, Fukuoka 816-8580, Japan.
*These authors contributed equally to this work.
†Corresponding author. Email: johnnyho@cityu.edu.hk

NW growth are provided in Materials and Methods. Briefly, by using one-step vapor-liquid-solid (VLS) growth process performed at ambient pressure (*16*, *17*), $InGaO_3(ZnO)_3$ superlattice NWs with well-defined morphology and average diameter of ~25 nm are successfully synthesized as shown in Fig. 1A and fig. S1. As compared to the layer-by-layer epitaxial growth processes (e.g., molecular beam epitaxy and pulse laser deposition) that are generally used to fabricate superlattice-structured complex oxide materials (*18*, *19*), the one-step ambient-pressure VLS method used here does not require complicated equipment for the experimental operation. In addition, because the as-synthesized $InGaO_3(ZnO)_3$ superlattice NWs are transferable on any substrate by well-developed contact printing schemes (fig. S1; with details described in Materials and Methods), there are no concerns about the compatibility of between the target device substrate and the NW growth process; thereby, devices can be even made on flexible plastics in a scalable and low-cost manner.

RESULTS

Structure and electrical characterizations of superlattice NWs

As a kind of "natural superlattice" (*20*), homologous compounds of $RMO_3(ZnO)_m$ (R = rare earth elements; M = Ga, Fe, or Al, etc.; m = integer) are easy to be crystallized with alternating stacks of RO_2^- layers and $MO(ZnO)_m^+$ blocks (space group $R\bar{3}m$, no. 166). In this case, the periodic dark-bright layered structures perpendicular to the NW radial direction are obviously witnessed in the high-resolution transmission electron microscopy (HRTEM) images as given in Fig. 1 (B and D), in which the dark contrast corresponds to the InO_2^- layers and the bright contrast correlates with the $GaO(ZnO)_3^+$ blocks (*21*). The corresponding diffraction spots appeared in a distinctive layered superlattice structure are as well found in the selected area electron diffraction (SAED) pattern (Fig. 1C). All the diffraction spots can be indexed as the $InGaO_3(ZnO)_3$ monoclinic structure. To be specific, the InO_2^- layer (In^{3+} locates at an octahedral site coordinated by O^{2-}) and the $GaO(ZnO)_3^+$ block (Ga^{3+} and Zn^{2+} share trigonal-bipyramidal and tetrahedral sites) (*19*) are alternately stacked along the *c* axis [0001] direction at a period of 13.8 Å (d_{0003}) as indicated in the HRTEM image in Fig. 1D, which is perpendicular to the growth direction [$1\bar{1}00$] of the $InGaO_3(ZnO)_3$ superlattice NWs, all together being in perfect agreement with the typical $InGaO_3(ZnO)_3$ crystal (JCPDS card, no. 40-0253). A total of 18 parallel stripe patterns with a periodic spacing of 13.8 Å are therefore calculated to have a length of 248.4 Å, which is well matched with the measured NW diameter of 25 nm, suggesting that the parallel stripe patterns distribute uniformly across the radial direction of the entire NW.

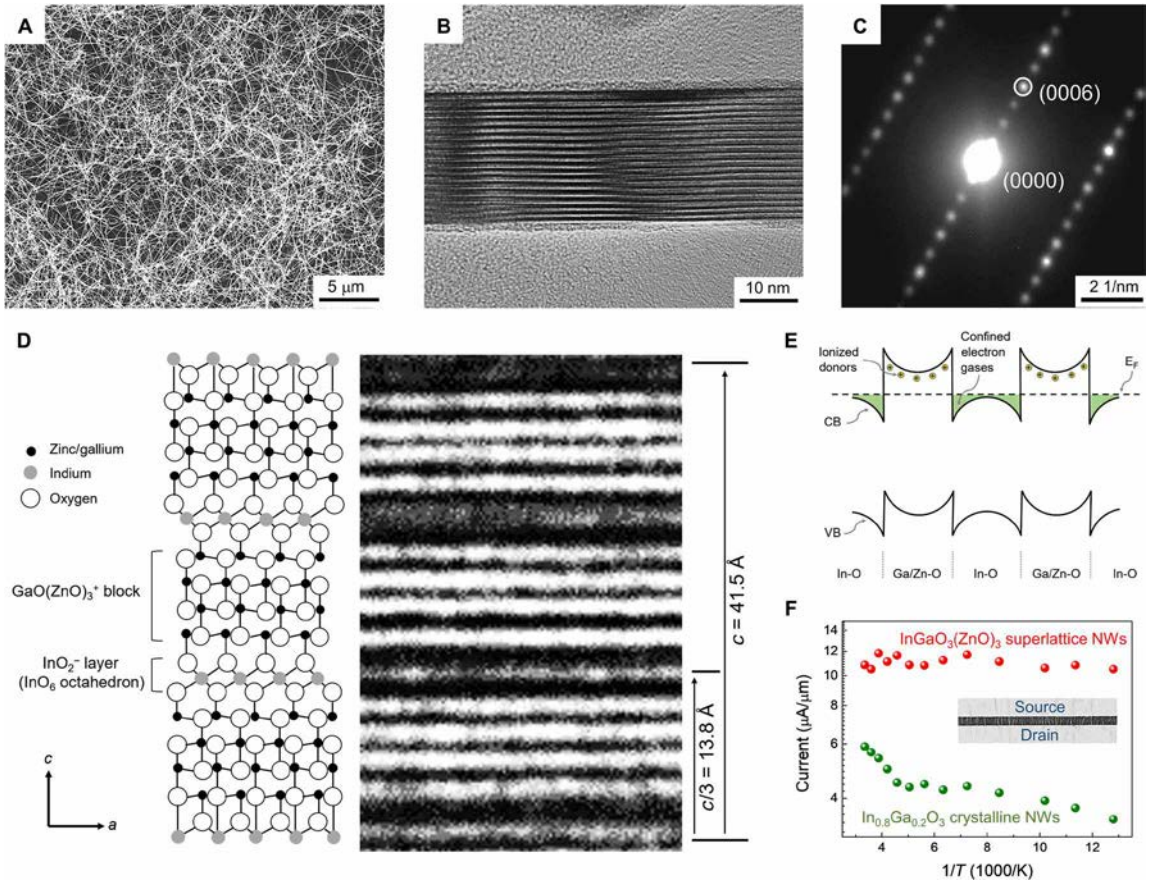

Fig. 1. Structure and electrical characterizations of $InGaO_3(ZnO)_3$ superlattice NWs. (**A**) Scanning electron microscopy (SEM) image of $InGaO_3(ZnO)_3$ superlattice NWs fabricated by Au-catalyzed VLS process at ambient pressure. (**B**) HRTEM image and (**C**) SAED pattern of a typical individual $InGaO_3(ZnO)_3$ superlattice NW. (**D**) Structural schematic of the $InGaO_3(ZnO)_3$ superlattice NW and its corresponding HRTEM image. (**E**) Qualitative energy-band diagram of quasi-2DEGs in the $InGaO_3(ZnO)_3$ superlattice. CB, VB, and EF are the abbreviations of conduction band, valence band, and Fermi level, respectively. (**F**) Temperature-related transport characterizations of $InGaO_3(ZnO)_3$ superlattice NWs (red points) and $In_{1.6}Ga_{0.4}O_3$ crystalline NWs (green points) with temperatures ranging from 78 to 298 K.

Energy-dispersive x-ray spectroscopy (EDS) analysis is also performed on the $InGaO_3(ZnO)_3$ NW as depicted in figs. S2 and S3, where the uniform elemental distribution and ideal In/Ga/Zn composition ratio of around 1:1:3 are observed. All these results explicitly elucidate the formation of layered superlattice structures of $InGaO_3(ZnO)_3$ NWs.

With the multiple quantum well structure, the $InGaO_3(ZnO)_3$ superlattice NWs are expected to have the effect of conduction band offset at heterointerfaces and corresponding carrier quantum confinement, which dictate the NW device performance (*18*). Since the conduction band edge of the InO_2^- layers lies in the energy level lower than the donor states of $GaO(ZnO)_3^+$ blocks, electrons from the $GaO(ZnO)_3^+$ blocks would transfer into the 2D InO_2^- layers when they are in contact (*22*). This spatial confinement of conductive electrons eventually leads to the band bending and the formation of quasi-2DEGs in the InO_2^- layers as illustrated in Fig. 1E. Further evidence supporting this carrier quantum-confinement effect can be provided by the temperature-dependent electrical measurement with temperatures ranging from 78 to 298 K once these NWs are transferred and fabricated into NW parallel arrayed field-effect transistor (FET) devices (Fig. 1F). It is evident that the carrier freeze-out behavior at low temperatures is absent in the $InGaO_3(ZnO)_3$ superlattice NWs, which is a characteristic indication of the trap-free temperature-independent carrier transport due to the existence of metallic-like quasi-2DEGs formed at the heterointerfaces (*23*). This is in distinct contrast to the typical temperature-activated transport behaviors of $In_{1.6}Ga_{0.4}O_3$ crystalline NWs (detailed material characterizations can be found in figs. S4 and S5), where the carrier density decreases exponentially with decreasing temperatures in the same temperature range. In addition, because the confined carriers are spatially separated from the donor sites, a reduction in ionized impurity scattering is realized in these two-dimensional InO_2^- layers, leading to the substantially improved carrier mobility of quasi-2DEGs (*22*). For the NW parallel arrayed devices, a typical field-effect electron mobility of 406 cm^2/Vs is obtained at 78 K by using $InGaO_3(ZnO)_3$ superlattice NWs as active channels. This low-temperature mobility value is substantially higher than the one of $In_{1.6}Ga_{0.4}O_3$ crystalline NWs (110 cm^2/Vs), suggesting that quasi-2DEG superlattice NWs are promising candidate building blocks for next-generation high-mobility electronics.

Device concept of quasi-2DEG photonic synapses

After that, these global back-gate FET devices based on parallel $InGaO_3(ZnO)_3$ superlattice NW arrays are further electrically characterized at different measurement conditions (Fig. 2A). Taking advantage of the surface chemical treatment of receiver substrates, controlled and uniform assembly of superlattice NWs into parallel arrays was realized by a simple contact printing process. As expected, all the individual device channels demonstrate the uniform distribution of NWs with an NW density of $1.5 \pm 0.1\ \mu m^{-1}$ (fig. S6). For directly examining the uniformity of device performance, transfer curves of 30 devices in a 6×5 array is measured, which exhibits an average on current of 6.54 μA/μm with a deviation of 0.37 μA/μm and an average hysteresis window (ΔV) of 38.07 V with a deviation of 4.01 V (fig. S7). These device performance parameters also highlight the uniformity of NW distribution in the parallel-NW array device. When measured in ambient atmosphere, the FET exhibits the classical n-type transfer characteristics with a moderate on/off current ratio of $>10^3$ and an obvious hysteresis window of ~40.6 V as depicted in Fig. 2B. Such electrical hysteresis is usually related to the charge trapping phenomena that occur at the NW surface defects (*24*, *25*). Evidently, there is a surface defect layer observed in the HRTEM image of obtained NWs (Fig. 2D), in which this defect layer is a typical feature associated with the VLS-grown NWs. In contrast, the hysteresis window of the FET device is notably reduced down to ~7.1 V, while the on current is considerably increased once the 10-nm-thick alumina (Al_2O_3) passivation is deposited onto the surface of $InGaO_3(ZnO)_3$ superlattice NWs (Fig. 2C). This hysteresis reduction suggests that the charge trapping events that occurred at surface defect sites (e.g., accepter-like defects or adsorbates) are the main reasons for the poor electrical conductivity and substantial hysteresis of NW devices (*25*). All these postulates can be further confirmed by the device transfer characteristics measured in vacuum with a pressure of $\sim 1 \times 10^{-4}$ Pa. Under vacuum, the device gives enhanced conductivity (~10^3 times larger at a gate bias of 0 V) together with excess carrier concentration that cannot be depleted completely to achieve the device off-state (i.e., the "always-on" behavior). The high-vacuum condition is always used to purposely remove the adsorbates away from NW surface defect layers and hence release the trapped charge carriers. After the NW devices have been stored in vacuum for more than 48 hours, the conductivity of the electron gases can be modulated from a semiconducting state to a metallic-like state. This finding reveals a slow adsorption process of adsorbates under vacuum conditions. When taking the devices out of vacuum and exposing them to ambient air again, the hysteresis loop of transfer curves slowly enlarges along with the exposing time from 0 to 12 hours. It takes roughly 12 hours for the hysteresis loop to revert back to its original state as shown in fig. S8. In any case, ohmic-like electrical contacts are found in the output characteristics of all measured devices in different conditions, which exclude the influence of contact resistances or oxygen/electrode interactions on electrical device measurements (fig. S9).

Meanwhile, on the basis of the wide-scan x-ray photoelectron spectroscopy (XPS) spectrum and O1s peak analysis in Fig. 2 (E and F), there is a dominant peak centered at 532.7 eV for the $InGaO_3(ZnO)_3$ superlattice NWs, in which the peak can be attributed to the existence of water and/or oxygen molecules adsorbed onto the NW surface. A control experiment of thermal heating–induced water molecule desorption (fig. S10) is also carried out to exclude the possibility of water molecules adsorbed onto NW surface layers acting as the charge trapping sites (with details described in text S1). In this case, the desorption of oxygen molecules from the NW surface is inferred to release the trapped electrons participating in the carrier transport, resulting in the enhanced conductivity of $InGaO_3(ZnO)_3$ superlattice NWs in vacuum. As discussed in previous reports, other external stimuli, such as light irradiation, can also lead to the oxygen desorption in quasi-2DEG systems. For instance, Meevasana *et al.* (*26*) found that the carrier density of a quasi-2DEG system can be controlled through exposing the $SrTiO_3$ surface to ultraviolet (UV) light, possibly as a result of light-mediated oxygen desorption from the $SrTiO_3$ surface. Thus, directly writing the surface states onto the quasi-2DEG NW surface using light could be an attractive route toward the efficient programming of their conductivity and widening of their functionality.

At this stage, to mimic the biological synapse, the photonic synapses based on $InGaO_3(ZnO)_3$ superlattice NW arrays are constructed. In this work, all the emulated synaptic behaviors of quasi-2DEG photonic synapses are demonstrated in ambient air. The conductivity of

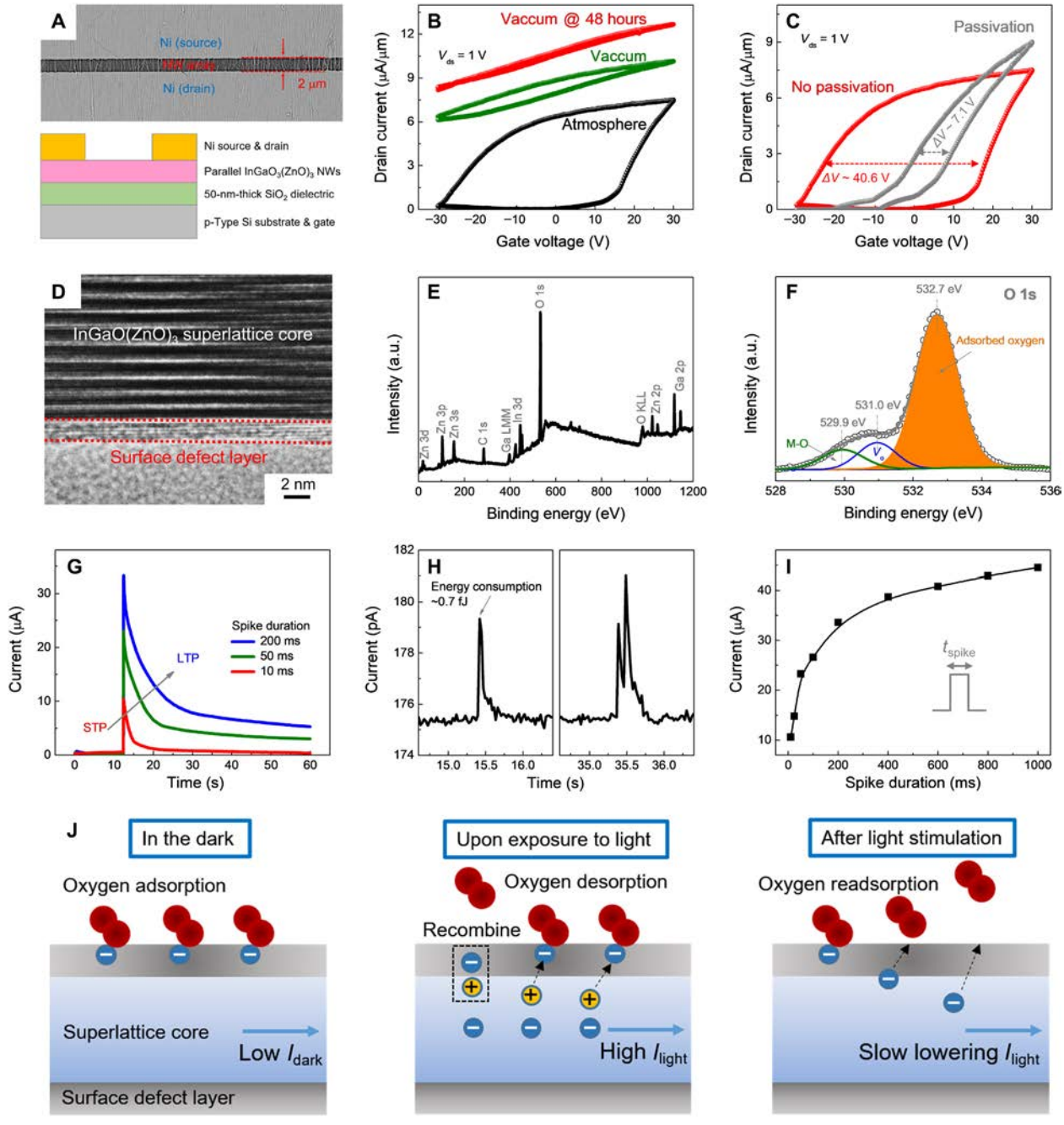

Fig. 2. Oxygen adsorption-desorption kinetics and strong carrier quantum-confinement effects on $InGaO_3(ZnO)_3$ superlattice NWs. (**A**) Schematic illustration and corresponding SEM image of the FET device based on $InGaO_3(ZnO)_3$ superlattice NW arrays with SiO_2 layer as the gate dielectric. (**B**) Transfer characteristics of the $InGaO_3(ZnO)_3$ NW array FET measured at different ambient and vacuum conditions. The scan rate is 500 mV/s. (**C**) Transfer characteristics of the $InGaO_3(ZnO)_3$ NW array FET before and after Al_2O_3 passivation measured at ambient atmosphere. The scan rate is 500 mV/s. (**D**) HRTEM image of a typical $InGaO_3(ZnO)_3$ NW with the distinct surface defect layer. (**E**) Wide scan XPS spectrum and (**F**) O 1s peak analysis of the $InGaO_3(ZnO)_3$ NWs. a.u., arbitrary units. (**G**) Light spike-induced EPSC generation and decaying characteristics of $InGaO_3(ZnO)_3$ NW arrays, demonstrating typical STP and LTP models. (**H**) EPSC triggered by a low-intensity presynaptic light spike (left) and short-term synaptic enhancement by two consecutive presynaptic light spikes (right) in 2DEG photonic synapses. (**I**) Spike duration–dependent plasticity of the $InGaO_3(ZnO)_3$ NW arrays with t_{spike} ranging from 10 to 1000 ms. (**J**) Schematics of oxygen adsorption–induced charge trapping and subsequent optically induced charge release on $InGaO_3(ZnO)_3$ superlattice NWs.

quasi-2DEG NW arrays is considered as a synaptic weight (or strength), while the light stimulus (261-nm UV light, 0.1 mW/cm^2) is considered as a presynaptic light spike. Under a bias voltage of 50 mV, light spikes with different duration times (t_{spike}) ranging from 10 to 1000 ms are used to trigger the excitatory postsynaptic current (EPSC). At a t_{spike} of 10 ms, the EPSC reaches a peak value of 10.6 μA and gradually decays back to its initial state within 10 s (Fig. 2G). Such EPSC behavior is quite similar to short-term plasticity (STP) in a biological

synapse (*27*). In another aspect, the transition behavior of STP to long-term plasticity (LTP) can also be mimicked. For example, by extending the t_{spike} to 200 ms, the EPSC of photonic synapses is further increased to a higher level (33.6 μA), while the EPSC can stay at a relatively high level for a long period after the spike, referring to a model known as LTP (*27*). In a particular case as shown in Fig. 2H (i.e., bias voltage ~0.1 mV, t_{spike} ~10 ms, and light density ~0.01 mW/cm^2), the energy dissipation of a single spike event is estimated to be ~0.7 fJ. The energy consumption for a single spike event is defined as the sum of electrical energy consumption ($I_{peak} \times t \times V$) and input light energy consumption ($P \times A \times t$) (with details described in text S2). Such subfemtojoule-level energy consumption is lower than that of biological synapses (~10 fJ per synaptic event) (*28*), complementary metal-oxide-semiconductor (CMOS) silicon neuromorphic circuits (~3000 fJ per synaptic event with an integration of 14 transistors and 3 capacitors) (*29*), and other hardware-based artificial synapses reported until now as summarized in table S1. The recorded low energy consumption of quasi-2DEG photonic synapses presented in this work is due to (i) the high mobility and high sensitivity of quasi-2DEG to various stimuli, (ii) the ultrahigh surface-to-volume ratio of $InGaO_3(ZnO)_3$ superlattice NWs that is critical for the oxygen adsorption-desorption kinetics, and (iii) the relatively short device channel length of 2 μm that reduces the path of energy dissipation. Scaling down the device dimensions and reducing the spike durations to submillisecond levels could be used as feasible strategies to further decrease the energy consumption per event.

Moreover, the spike duration–dependent plasticity of quasi-2DEG photonic synapses is also studied as depicted in Fig. 2I and fig. S11. The measured EPSC peak values increase from 10.6 μA all the way to 44.5 μA with t_{spike} spanning from 10 to 1000 ms. From a view point of charge-storage accumulative photoelectric effect (*25*), the $InGaO_3(ZnO)_3$ superlattice NW arrays could break the power law dependence of conventional photodetectors ($I_{ph} \sim P^{\alpha}$) (*30*), following the time-dependent exponential-association photoelectric conversion law [$I_{ph} \sim a \cdot (1 - e^{-b \cdot P \cdot t})$], in which more charge carriers can be accumulated in the NWs through the longer light exposure and thus giving rise to the higher responsivities and detectivities of photodetectors (with details described in text S3). Importantly, with a duration time of 1000 ms, quasi-2DEG photonic synapses exhibit a high responsivity of 1.05×10^6 A/W and a high detectivity of 3.15×10^{13} Jones (fig. S12). All these performance parameters are already comparable to those of state-of-the-art low-dimensional semiconductor-based photodetectors (table S2). Generally, the responsivity measures the input-output gain, while the detectivity represents the sensitivity of a detector system. These superior sensing parameters directly indicate that quasi-2DEG devices presented in this work would accurately and efficiently detect external light stimuli.

To better understand the device operation mechanism, simplified schematic diagrams are used and illustrated in Fig. 2J, in which oxygen adsorption–induced charge trapping and subsequent optically induced charge release are highlighted (with details described in text S4). The biological synapse changes its conductance by exchanging Ca^{2+} ions when the spike stimulus arrives, while the quasi-2DEG synaptic devices presented here change its conductance by regulating the number of adsorbed oxygen according to the applied light pulse. This shows the potential of building artificial neuromorphic devices using such strongly electron-correlated quasi-2DEG superlattice NWs. In addition, we should note that owing to the strong carrier quantum-confinement effects at superlattice heterointerfaces, quasi-2DEGs are highly sensitive to the applied electrostatic fields (*8*, *11*, *31*). When the light-mediated surface states induce the associated electrostatic fields, channel conductance can be precisely identified as a result of the altered carrier confinement. In this case, it is incredible to build a truly brain-like cognitive system by using quasi-2DEG systems, using the oxygen adsorption-desorption kinetics on the NW surface and the strong carrier quantum-confinement effects in the superlattice core, which has bionic performance that is unreachable by other conventional semiconductors.

Brain-like functions of flexible quasi-2DEG photonic synapses

In contrast to the conventional complex oxide materials fabricated on rigid substrates (e.g., single-crystalline yttria-stabilized zirconia substrate) by epitaxial growth (*18*, *19*), $InGaO_3(ZnO)_3$ superlattice NWs presented here also have a great deal of interest to be integrated on plastic substrates to achieve mechanically flexible brain-like electronics. To demonstrate the possible implementation of $InGaO_3(ZnO)_3$ superlattice NWs for flexible neuromorphic systems, the entire device fabrication procedure is transferred onto a polyimide substrate (Fig. 3A). The flexible quasi-2DEG photonic synapses are then electrically characterized before and after 100 successive mechanical bending cycles with a bending radius of ~5 mm (fig. S13). It is noted that the EPSC measurements do not reveal any substantial changes, demonstrating the decent mechanical stability arising from the unique NW morphology. The flexible quasi-2DEG photonic synapses have the potential to be merged with other research fields ranging from wearable AI systems to personalized health care in the near future.

In biological systems, synapses can update their synaptic weight according to the history of the stimulation, which is important for decoding temporal information (*27*). For example, in a typical synaptic plasticity called paired-pulse facilitation (PPF), synapses can fill in their synaptic weight based on the timing between paired spikes (*32*). In this case, to mimic the PPF behavior in our flexible quasi-2DEG photonic synapses, two consecutive presynaptic light spikes (0.1 mW/cm^2, 10 ms) with interspike interval (Δt_{pre}) ranging from 200 to 2000 ms are applied onto the $InGaO_3(ZnO)_3$ superlattice NWs. As depicted in Fig. 3B, the peak intensity value of EPSC triggered by the second light spike (Δt_{pre} = 200 ms) is much larger than that by the first one, which is a characteristic indication of PPF behavior. This bionic PPF phenomenon is attributed to the spatially separated photoexcited states that contribute to the synaptic weight of the quasi-2DEG photonic synapses. After the first light spike, photogenerated electrons will diffuse gradually back to their equilibrium position on the NW surface. If the second light spike is applied at this time with a smaller Δt_{pre}, photo-generated electrons triggered by the first spike are still partially residing in superlattice NW cores, contributing to the synaptic weight. Under this condition, EPSCs triggered by the second spike are augmented, which induces the PPF behavior. The PPF index, defined as the ratio of the amplitudes between the second EPSC peak (A2) and the first EPSC peak (A1), is plotted as a function of Δt_{pre} in Fig. 3C. It is obvious that a higher PPF index value can be obtained when the applied paired spikes have a shorter Δt_{pre}. When Δt_{pre} is 200 ms, a maximum PPF index value of 210% is witnessed (Fig. 3A), which is substantially larger than most of the reported artificial synapses (table S3). This finding indicates that the flexible quasi-2DEG photonic synapses have the outstanding ability to decode temporal information. Apart from the temporal related plasticity discussed above, light intensity–dependent plasticity

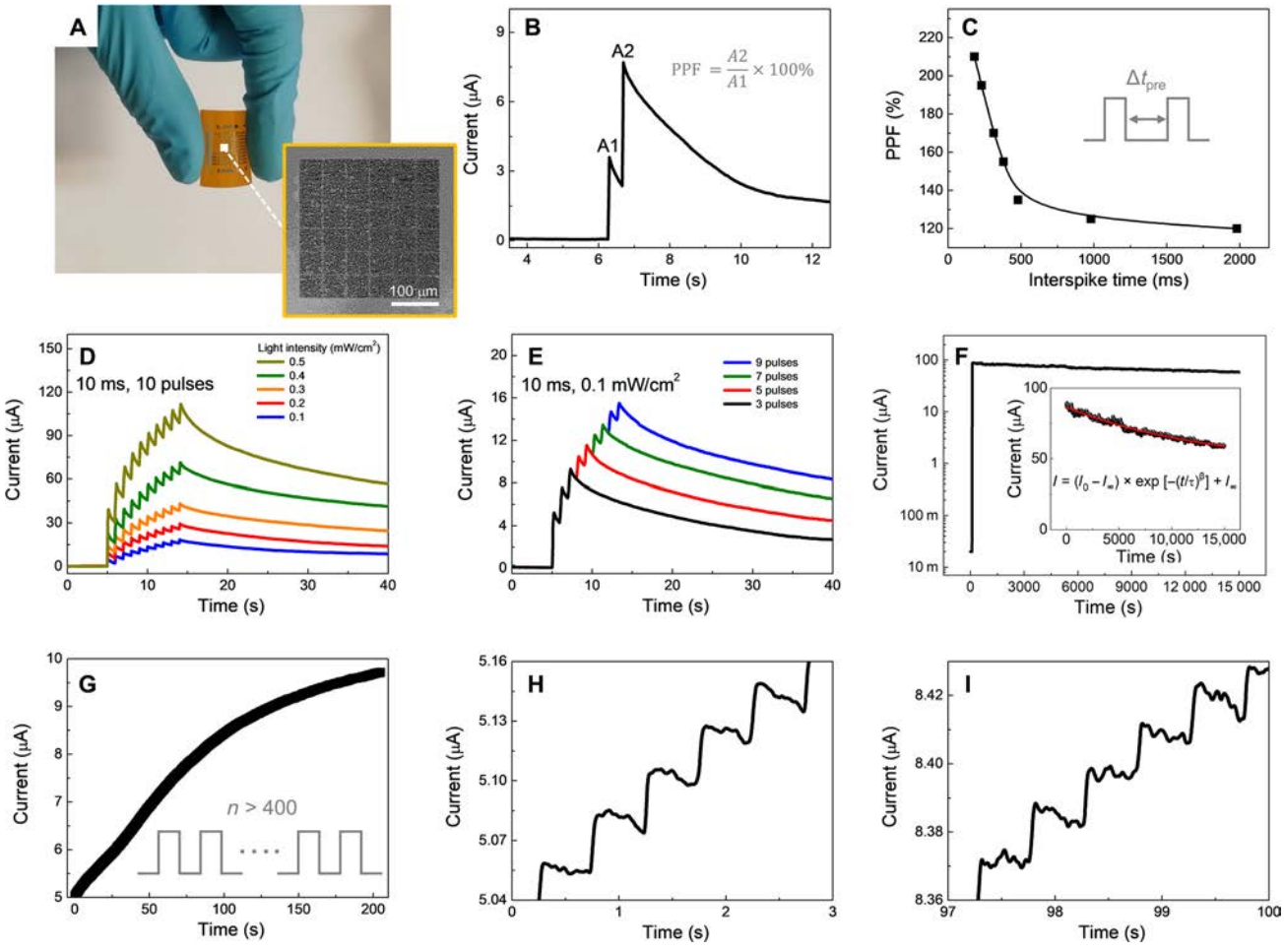

Fig. 3. Brain-like information processing, nonvolatile charge retention, and multibit-level memory functions of flexible quasi-2DEG photonic synapses. (**A**) Photograph of flexible quasi-2DEG photonic synapse devices based on polyimide substrates. Inset shows the corresponding SEM image of the fabricated 6 × 5 device array. Photo credits: You Meng, City University of Hong Kong. (**B**) Paired-pulse facilitation (PPF) behavior of a typical quasi-2DEG photonic synaptic device. (**C**) PPF index, defined as the ratio of A2/A1, plotted as a function of interspike time. (**D**) Light intensity–dependent plasticity of quasi-2DEG photonic synapses at a constant spike time of 10 ms for 10 pulses with light intensity ranging from 0.1 to 0.5 mW/cm^2. (**E**) Pulse number–dependent plasticity of quasi-2DEG photonic synapses at a constant spike time of 10 ms and light intensity of 0.1 mW/cm^2 with the pulse number ranging from 3 to 9. (**F**) Giant PPC phenomenon in $InGaO_3(ZnO)_3$ superlattice NW arrays with the nonvolatile charge retention time using logarithm *y* coordinate and (inset) linear *y* coordinate. (**G** to **I**) Multibit storage properties of $InGaO_3(ZnO)_3$ superlattice NW arrays with more than 400 conductance states are continuously programed by laser pulses.

(Fig. 3D) and pulse number–dependent plasticity (Fig. 3E) are also successfully demonstrated on our flexible quasi-2DEG photonic synapses, suggesting a more active role in precisely defining their synaptic weight according to the optical cues with different spike durations, intensities, or pulses.

To examine the dynamic potentiation and depression behaviors of quasi-2DEG synapses, sequential photonic/electric pulses are used as the presynaptic input signals. Specifically, the sequential photonic pulses (amplitude, 0.05 mW/cm^2; duration, 10 ms; interval, 1 s) are applied onto the device to increase the EPSC gradually, realizing the optical potentiation function. On the other hand, sequential negative electric pulses (amplitude, −5 V; duration, 10 ms; interval, 1 s) are applied onto the gate terminal to mimic the electronic suppression function. Similar strategies that involve light-induced potentiation and electronic-induced suppression have been reported by several recent works (*33*–*35*). While under a negative gate voltage, more electrons are concentrated at the NW surface and captured by oxygen molecules (O_2) adsorbed onto the NW surface: $O_2(g) + e^- \rightarrow O_2^-(ad)$. The adsorbed oxygen would deplete the $InGaO_3(ZnO)_3$ NW and make it with relatively low conductivity. In this regard, the synaptic depression (erase) operation in our quasi-2DEG synapses can be realized by simply applying negative gate voltage pulses. As shown in fig. S14, the monitored EPSC increases stepwise to 2.94×10^5 A by varying the 100 light pulse sequences and then drops back to 2.48×10^7 A by applying the 100 positive voltage pulse sequences. All of the positive and negative exponentially varied EPSC responses indicate the potentiation and depression behavior of the quasi-2DEG synapses.

Spike timing–dependent plasticity (STDP) is of importance to the Hebbian synaptic learning and memory functions, where it is evaluated by the time interval and the spike order of the pre- and postsynaptic stimulations. In this investigation, the STDP of quasi-2DEG synapses is carried out by applying two separated input signals from the gate terminal (as presynaptic spikes) and the light stimuli (as postsynaptic spikes), respectively. The spike interval time (ΔT),

defined as $T_{post\text{-}spike} - T_{pre\text{-}spike}$, ranges from 100 to 900 ms. As presented in the corresponding schematic in fig. S15A, the presynaptic signal is composed of a larger negative voltage pulse (−10 V, 100 ms) and a smaller positive voltage pulse (+5 V, 100 ms) for the better symmetry of the STDP. To detect the synaptic weight change, a read voltage of 10 mV is applied onto the drain electrode. The relative change in conductivity represents the variation of synaptic weight (ΔW), which achieves the largest value once ΔT goes to zero. The obtained results of the potentiation ($\Delta T > 0$) and the depression ($\Delta T < 0$) responses are then illustrated in fig. S15B, where the relationship between ΔW and ΔT can be fitted with an exponential function, being highly similar to that of biological synapses.

The flexible quasi-2DEG photonic synapses could go beyond purely mimicking the brain-like information processing by also implementing a human memory model (*1*, *28*). As given in Fig. 3F, when an intensive light stimulation (1 mW/cm^2, 10 s) is applied onto the $InGaO_3(ZnO)_3$ NWs, the giant PPC phenomenon with a light-to-dark current ratio of ~5×10^3 is observed. With the aim to minimize the influence of read voltage on the charge retention, a small read voltage of 10 mV is used in the charge retention measurement. The retention loss in the quasi-2DEG photonic synapses bears many similarities to the memory loss in biological systems. The fitting result in Fig. 3F indicates that the current decay process accords well with the Kohlrausch stretched exponential function (*32*, *36*, *37*)

$$I = (I_0 - I_\infty) \times \exp\left[-(t/\tau)^\beta\right] + I_\infty$$

where I_0 is the triggered EPSC at the end of the presynaptic spike, I_∞ is the final value of the decay current, and τ and β denote the relaxation time constant and the stretching exponent, respectively. The value of τ is fitted to be ~1.3×10^4 s, suggesting a good nonvolatile charge retention characteristic, being better than those of the recently reported ITO/Nb:$SrTiO_3$ Schottky junction synaptic memristors ($\tau \sim 1.2 \times 10^4$ s) (*37*) and the native oxide–inspired InSe synaptic transistors (retention time ~10^4 s) (*35*). Owing to the simultaneously coexisted photodetector and memory functions of quasi-2DEG photonic synapses, there is no need to construct additional nonvolatile memory arrays for charge storage in an image sensing chip based on $InGaO_3(ZnO)_3$ superlattice NWs, which is beneficial for the energy efficiency, scalability, and fabrication cost of integrated visual systems.

On the other hand, the multibit data storage capability of $InGaO_3(ZnO)_3$ NWs is also evaluated. As shown in Fig. 3G, the quasi-2DEG photonic synapse is exposed to successive light pulses (0.05 mW/cm^2, 10 ms) at intervals of 0.5 s, leading to a progressive EPSC increase controlled by the number of pulses. This progressive increase signifies the direct writing of surface states onto the quasi-2DEG NW surface and the continuous injection of electrons into the superlattice NW core. This way, the optoelectronic memory with 400 distinct programmable states can be successfully demonstrated (Fig. 3, G to I, and fig. S16), which is equivalent to a data storage ability over 8 bits (i.e., 256 programmable states). This observation is akin to a well-studied biological process, posttetanic potentiation, in which if many stimuli follow closely one after another, the synaptic transmission would gradually grow with the increasing number of stimuli. In this manner, the existing biological synaptic facilitation model that describes the transmitter release dynamics during repetitive stimulation (*38*) could be used to predict or distinguish these conductance states (or synaptic weights) of the quasi-2DEG synapses (fig. S17; with details described in text S5). In general, the learning and memory functions in human brain are contributed by the dynamic change of synaptic connections (*27*). For an artificial neuromorphic system, the long-term storage lifetime and the gradual modulation of hundreds of programmable states could enable high learning efficiency and capacity that are useful for brain-like adaptive learning on indeterministic information (*2*, *28*).

Quasi-2DEG artificial visual system

Since the quasi-2DEG photonic synapses are capable of high-performance light detection, brain-like information processing, and multibit-level data storage, all these functionalities can be combined together and implemented as human visual systems (Fig. 4A). In visual systems, orientation selectivity is a well-known biological function of the primary visual cortex that is necessary for encoding of visual images (*1*, *39*). In the primary visual cortex, neurons respond preferentially to edges with a particular orientation of input patterns, which is ascribed to the feed-forward filtering function that causes weight enhancement near the preferred orientation (*39*). To imitate the orientation selectivity in the primary visual cortex, a special experimental setup is established for the orientation dependence experiment in the attended conditions. In detail, a square panel with 10 pairs of black-white grating patterns (each light-tight black and transparent white stripes with a width of 0.5 cm) is placed perpendicular to the incident light, irradiating on the device, with a controlled lateral movement at a fixed speed (v) of 1 cm/s (Fig. 4B). On top of the lateral movement, the grating stripes can also be rotated to have different orientation angles of θ with respect to the incident light (Fig. 4B, inset). When the stripes are located vertically, the θ value is defined as 0°. Once the stripes rotate in a clockwise direction or in an anticlockwise direction, the θ value increases or decreases accordingly. Hence, for each grating orientation angle, when the edge of a transparent white stripe moves across the incident light during the lateral motion, the presynaptic terminal of quasi-2DEG photonic synapses would receive a light pulse signal. The visual response is referred to the maximum EPSC peak value at each orientation angle (fig. S18). In explicit, when the orientation is set at 0°, 10 presynaptic light spikes are triggered successively, inducing a set of markedly increasing EPSC peaks with a maximum value of 6.47 μA (Fig. 4D). When the orientation angle is changed to 72°, only four presynaptic light spikes are triggered, giving four EPSC peaks with a maximum value of 2.55 μA (Fig. 4E). These visual responses of quasi-2DEG photonic synapses are then plotted as a function of the orientation angle θ (Fig. 4C). Following the typical neuroscience protocol (*40*), the half-width measured at half-maximum height (HWHM) of the fitting curve is used as a criterion of orientation selectivity. In this work, the HWHM value is estimated to be 45°, which is comparable to some biological experiments on monkey visual cortex (*41*). Moreover, suppressed visual responses in the "unattended" mode relative to the "attended" mode are also successfully demonstrated in Fig. 4C. To add extra irrelevant stimuli to orientation selectivity studies in the unattended conditions, the incident light is further mechanically chopped with a frequency of 100 Hz (fig. S19). Although unattended mode suppresses the visual responses of quasi-2DEG photonic synapses, the selectivity measured by the HWHM of its orientation-tuning curve does not get obviously altered. Overall, although there have been some pioneer simulation works about the orientation selectivity on artificial synapses (*42*–*44*), here in our work, the orientation selectivity is fully experimentally demonstrated on a

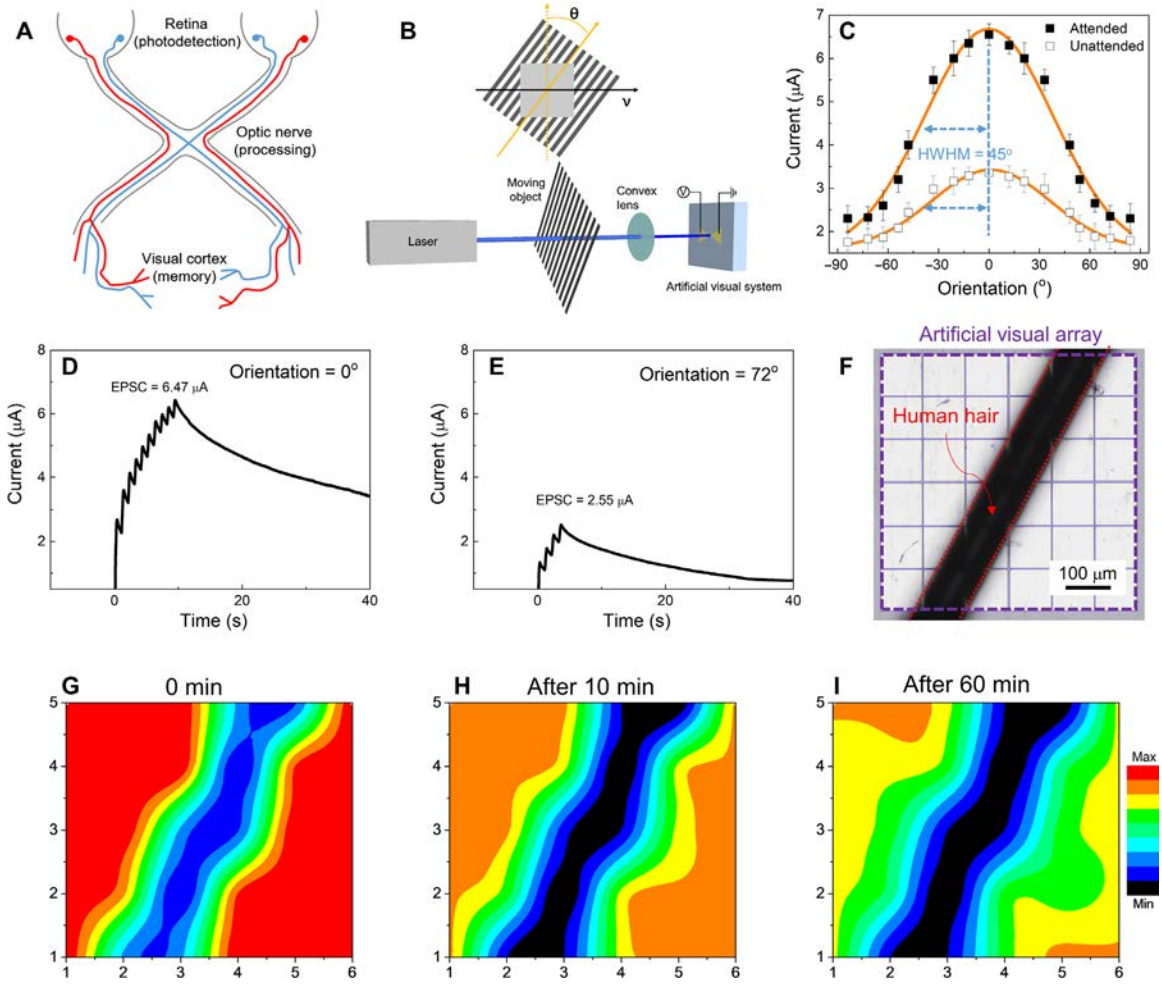

Fig. 4. Artificial visual system based on flexible quasi-2DEG photonic synapse arrays. (**A**) Schematic diagram of the human visual system, consisting of retina, visual nerve, and primary visual cortex. (**B**) Schematic diagram for the experimental setup of the attended orientation selectivity. (**C**) Attended and unattended visual responses of quasi-2DEG photonic synapses plotted as a function of the orientation angle. The solid line represents the Gaussian fitting curve as a guide to the eye. (**D** and **E**) Visual responses of quasi-2DEG photonic synapses with orientation angles of 0° and 72°, respectively. (**F**) Optical micrograph of the artificial visual system based on quasi-2DEG photonic synapse arrays. A human hair with a diameter of ~80 μm was used to pattern the light. (**G** to **I**) Imaging and memorizing behaviors of the artificial visual system after different retention time.

real moving object, which is extremely meaningful to hardware applications toward visual information detection and processing.

To further shed light on the functionality and scalability of these devices, an artificial visual system, consisting of a 6 × 5 pixel array (i.e., total 30 devices), is fabricated to record the information of the applied patterned light. As an individual pixel has a feature size of 100 μm in our artificial visual system, a pixel density of 254 pixels per inch is achieved. Such high pixel density makes our quasi-2DEG artificial visual system able to recognize very tiny objects. This pixel size is substantially smaller than those of previously reported artificial visual systems, such as the pixel size of 250 μm in two-terminal MoO_x optoelectronic resistive random access memory arrays (*45*) and the pixel size of about millimeter level in artificial flexible visual memory system using UV-motivated memristors (*46*). As depicted in Fig. 4F, a human hair with diameter around 80 μm is used to pattern light. This way, only devices exposed under the patterned light can be triggered. After removing the light, a clear hair-shaped pattern can be observed from the EPSC mapping in Fig. 4G that read directly from the quasi-2DEG visual system (fig. S20). This system not only can detect optical patterns but also can store them for later read out. For example, after powering off the devices for 1 hour, the visual memory arrays can still retain the hair-shaped pattern with little attenuation (Fig. 4, H and I), demonstrating the capability of imaging, data processing, and memorizing here. To reveal the real-time imaging and memorization capabilities of our artificial visual system, a movie file is provided (fig. S21 and movie S1). In the future, a higher pixel density can be used to distinguish more sophisticated patterns.

DISCUSSION

We propose, design, and demonstrate the quasi-2DEG photonic synapses on the basis of $InGaO_3(ZnO)_3$ superlattice NWs using an unreported device operation concept by combining the oxygen adsorption-desorption kinetics on the NW surface and the strong

carrier quantum-confinement effects in the superlattice core. Unlike traditional computing architectures with physically separated data processing and memorizing units, our quasi-2DEG photonic synapses could process information in an in-memory computing approach with an ultralow energy consumption down to subfemtojoule per synaptic event. During the programming process, the photo-generated electrons can efficiently transfer into superlattice NW cores, leading to the storage of localized electrons in multiple quantum wells, which results in the persistent charge retention and the multibit-level memory capability. By regulating the number of adsorbed oxygen or trapped electrons through the applied light pulse, resembling the Ca^{2+} ions flux and neurotransmitter release dynamics in biological synapses, we can achieve a truly brain-like cognitive system to perform data-intensive tasks such as orientation selectivity and image memorizing. All these results can evidently provide a promising device scheme to build artificial neuromorphic systems using quasi-2DEG in future applications of bionic devices, electronic eyes, multifunctional robotics, etc.

MATERIALS AND METHODS

Material synthesis

In this work, $InGaO_3(ZnO)_3$ superlattice NWs were grown on 50-nm-thick SiO_2/Si substrates by an ambient-pressure chemical vapor deposition (CVD) method. Au film (0.1 nm thick) was deposited on the substrates as catalyst by using thermal evaporation. For the preparation of precursor source of $InGaO_3(ZnO)_3$ superlattice NWs, Ga granules (1 to 2 mm in size; 99.999% in purity, China Rare Metal), In granules (99.999%, China Rare Metal), zinc powder (>99.8%, Sigma-Aldrich), and graphite powder (0.3 g, <20 μm in size, synthetic; Sigma-Aldrich) were mixed together and annealed at 250°C for 30 min at atmosphere before placing into a tube furnace. The as-prepared precursor source was placed at the sealed end of a quartz tube (10 cm in length and 1 cm in diameter), while the substrate was positioned 2 cm away from the source in the same quartz tube. This quartz tube was then put in the center of a large quartz tube (1 inch in diameter) within the single-zone tube furnace. During the growth, the setup was heated up to 990°C in 20 min and held for 10 min with the flow rate of gas mixture (10% oxygen, +90% argon) and argon (99.9995%) maintained at 20 and 80 sccm, respectively. When the growth was completed, the CVD system was naturally cooled to the room temperature.

Material characterization

The morphologies of as-prepared NWs were examined using scanning electron microscopy (SEM, Quanta 450 FEG, FEI) and transmission electron microscopy (TEM, CM 20). HRTEM (JEOL-2001F) and SAED were also performed to assess the crystallinity of the NWs. EDS and elemental mappings were used to evaluate the chemical composition of the NWs. XPS was performed with a VG MultiLab 2000 (Thermo Fisher Scientific, Waltham, MA) photoelectron spectrometer. All of the binding energies were referenced to the C 1s peak at 284.8 eV of the surface adventitious carbon.

Contact printing

Taking advantage of the surface chemical treatment of receiver substrates, controlled and uniform assembly of superlattice NWs into parallel arrays was realized by a simple contact printing process. In detail, our NW contact printing method was operated by the directional sliding of a growth substrate, consisting of a lawn of NWs, on top of a receiver substrate (i.e., p-type Si/SiO_2 substrate or flexible PI substrate) as demonstrated in fig. S1. Before printing, the receiver substrate was pretreated with poly-L-lysine to manipulate the adhesion interaction between NWs and receiver substrates during the sliding process. Besides, the donor (growth) substrate was cut into the desired dimension and mounted on a metal weight, with the aim to provide a uniform pressure of ~30 g/cm^2. During the printing process, the donor substrate (with the weight) was then pushed and slid against the receiver substrate by a micromanipulator with a constant velocity of ~10 mm/min. Eventually, NWs were anchored by the van der Waals interaction with the surface of the receiver substrate, resulting in the direct transfer of aligned NWs onto the receiver substrate.

Device fabrication and electrical measurement

For the device fabrication, the as-fabricated NWs were transferred onto the p-type Si substrates with a 50-nm-thick thermally grown oxide layer by using dry transfer technique, followed by standard photolithography to define the source and drain electrode regions (fig. S22). Then, electron beam evaporation was used to deposit the 80-nm-thick Ni film. The lift-off process was subsequently performed to obtain the source and drain electrodes. The detailed description of the NW array device fabrication is schematically presented in fig. S22. At the end, electrical performance of the fabricated NW devices was evaluated by using a standard probe station with an Agilent 4155C semiconductor analyzer (Agilent Technologies, Santa Clara, CA, USA). Temperature-related electrical measurements were carried out under high vacuum (~1×10^{-4} Pa) at temperature ranging from 78 to 298 K using a cryogenic probe station. All the transfer curves were measured at a scan rate of 500 mV/s, with a hold time of 1 s and a delay time of 100 ms. Field-effect mobility (μ_{FE}) in the linear regime were calculated using the equation $\mu = L^2 g_m/(C_g V_d)$, where L is the channel length, g_m is transconductance (defined as dI_{ds}/dV_{gs}), and C_g is the gate capacitance. The value of C_g is obtained from the finite element analysis software COMSOL tailored for the cylinder on-plane model. A UV laser with a wavelength of 261 nm was used in the experiment for the optical stimuli. To demonstrate the image memorization of the artificial visual system, we used human hair as optical mask, and each pixel was illuminated and measured one by one.

SUPPLEMENTARY MATERIALS

Supplementary material for this article is available at http://advances.sciencemag.org/cgi/content/full/6/46/eabc6389/DC1

REFERENCES AND NOTES

1. E. R. Kandel, J. H. Schwartz, T. M. Jessell, S. A. Siegelbaum, A. J. Hudspeth, *Principles of Neural Science* (McGraw-Hill New York, 2000).
2. L. F. Abbott, W. G. Regehr, Synaptic computation. *Nature* **431**, 796–803 (2004).
3. B. C.-K. Tee, A. Chortos, A. Berndt, A. K. Nguyen, A. Tom, A. M. Guire, Z. C. Lin, K. Tien, W.-G. Bae, H. Wang, P. Mei, H.-H. Chou, B. Cui, K. Deisseroth, T. N. Ng, Z. Bao, A skin-inspired organic digital mechanoreceptor. *Science* **350**, 313–316 (2015).
4. L. E. Osborn, A. Dragomir, J. L. Betthauser, C. L. Hunt, H. H. Nguyen, R. R. Kaliki, N. V. Thakor, Prosthesis with neuromorphic multilayered e-dermis perceives touch and pain. *Sci. Robot.* **3**, eaat3818 (2018).
5. Y. Kim, A. Chortos, W. Xu, Y. Liu, J. Y. Oh, D. Son, J. Kang, A. M. Foudeh, C. Zhu, Y. Lee, S. Niu, J. Liu, R. Pfattner, Z. Bao, T.-W. Lee, A bioinspired flexible organic artificial afferent nerve. *Science* **360**, 998–1003 (2018).
6. J. Mannhart, D. G. Schlom, Oxide interfaces–an opportunity for electronics. *Science* **327**, 1607–1611 (2010).
7. R. Ramesh, D. G. Schlom, Creating emergent phenomena in oxide superlattices. *Nat. Rev. Mater.* **4**, 257–268 (2019).

8. A. D. Caviglia, S. Gariglio, N. Reyren, D. Jaccard, T. Schneider, M. Gabay, S. Thiel, G. Hammerl, J. Mannhart, J.-M. Triscone, Electric field control of the $LaAlO_3/SrTiO_3$ interface ground state. *Nature* **456**, 624–627 (2008).
9. A. Tsukazaki, A. Ohtomo, T. Kita, Y. Ohno, H. Ohno, M. Kawasaki, Quantum hall effect in polar oxide heterostructures. *Science* **315**, 1388–1391 (2007).
10. A. Tsukazaki, S. Akasaka, K. Nakahara, Y. Ohno, H. Ohno, D. Maryenko, A. Ohtomo, M. Kawasaki, Observation of the fractional quantum Hall effect in an oxide. *Nat. Mater.* **9**, 889–893 (2010).
11. P. Irvin, Y. Ma, D. F. Bogorin, C. Cen, C. W. Bark, C. M. Folkman, C.-B. Eom, J. Levy, Rewritable nanoscale oxide photodetector. *Nat. Photonics* **4**, 849–852 (2010).
12. D. Miron, D. Cohen-Azarzar, B. Hoffer, M. Baskin, S. Kvatinsky, E. Yalon, L. Kornblum, Oxide 2D electron gases as a reservoir of defects for resistive switching. *Appl. Phys. Lett.* **116**, 223503 (2020).
13. H. Chen, Y. S. Rim, I. C. Wang, C. Li, B. Zhu, M. Sun, M. S. Goorsky, X. He, Y. Yang, Quasi-two-dimensional metal oxide semiconductors based ultrasensitive potentiometric biosensors. *ACS Nano* **11**, 4710–4718 (2017).
14. A. Tebano, E. Fabbri, D. Pergolesi, G. Balestrino, E. Traversa, Room-temperature giant persistent photoconductivity in $SrTiO_3/LaAlO_3$ heterostructures. *ACS Nano* **6**, 1278–1283 (2012).
15. B. Tian, C. M. Lieber, Nanowired bioelectric interfaces. *Chem. Rev.* **119**, 9136–9152 (2019).
16. F. Li, S. P. Yip, R. Dong, Z. Zhou, C. Lan, X. Liang, D. Li, Y. Meng, X. Kang, J. C. Ho, Crystalline InGaZnO quaternary nanowires with superlattice structure for high-performance thin-film transistors. *Nano Res.* **12**, 1796–1803 (2019).
17. F. Li, Y. Meng, R. Dong, S. P. Yip, C. Lan, X. Kang, F. Wang, K. S. Chan, J. C. Ho, High-performance transparent ultraviolet photodetectors based on InGaZnO superlattice nanowire arrays. *ACS Nano* **13**, 12042–12051 (2019).
18. H. Ohta, K. Nomura, M. Orita, M. Hirano, K. Ueda, T. Suzuki, Y. Ikuhara, H. Hosono, Single-crystalline films of the homologous series $InGaO_3(ZnO)_m$ grown by reactive solid-phase epitaxy. *Adv. Funct. Mater.* **13**, 139–144 (2003).
19. K. Nomura, H. Ohta, K. Ueda, T. Kamiya, M. Hirano, H. Hosono, Thin-film transistor fabricated in single-crystalline transparent oxide semiconductor. *Science* **300**, 1269–1272 (2003).
20. K. Nomura, H. Ohta, K. Ueda, T. Kamiya, M. Orita, M. Hirano, T. Suzuki, C. Honjyo, Y. Ikuhara, H. Hosono, Growth mechanism for single-crystalline thin film of $InGaO_3(ZnO)_5$ by reactive solid-phase epitaxy. *J. Appl. Phys.* **95**, 5532–5539 (2004).
21. D. L. Huang, L. L. Wu, X. T. Zhang, Size-Dependent $InAlO_3(ZnO)_m$ nanowires with a perfect superlattice structure. *J. Phys. Chem. C* **114**, 11783–11786 (2010).
22. H. Faber, S. Das, Y.-H. Lin, N. Pliatsikas, K. Zhao, T. Kehagias, G. Dimitrakopulos, A. Amassian, P. A. Patsalas, T. D. Anthopoulos, Heterojunction oxide thin-film transistors with unprecedented electron mobility grown from solution. *Sci. Adv.* **3**, e1602640 (2017).
23. J. Z. Li, J. Y. Lin, H. X. Jiang, M. Asif Khan, Q. Chen, Persistent photoconductivity in a two-dimensional electron gas system formed by an AlGaN/GaN heterostructure. *J. Appl. Phys.* **82**, 1227–1230 (1997).
24. N. Han, F. Wang, J. J. Hou, S. P. Yip, H. Lin, F. Xiu, M. Fang, Z. Yang, X. Shi, G. Dong, T. F. Hung, J. C. Ho, Tunable electronic transport properties of metal-cluster-decorated III-V nanowire transistors. *Adv. Mater.* **25**, 4445–4451 (2013).
25. Z. Shao, T. Jiang, X. Zhang, X. Zhang, X. Wu, F. Xia, S. Xiong, S.-T. Lee, J. Jie, Memory phototransistors based on exponential-association photoelectric conversion law. *Nat. Commun.* **10**, 1294 (2019).
26. W. Meevasana, P. D. C. King, R. H. He, S.-K. Mo, M. Hashimoto, A. Tamai, P. Songsiriritthigul, F. Baumberger, Z.-X. Shen, Creation and control of a two-dimensional electron liquid at the bare $SrTiO_3$ surface. *Nat. Mater.* **10**, 114–118 (2011).
27. W. Gerstner, W. M. Kistler, *Spiking Neuron Models: Single Neurons, Populations, Plasticity* (Cambridge Univ. Press, 2002).
28. D. Kuzum, S. Yu, H.-S. Philip Wong, Synaptic electronics: Materials, devices and applications. *Nanotechnology* **24**, 382001 (2013).
29. J. Park, M.-W. Kwon, H. Kim, S. Hwang, J.-J. Lee, B.-G. Park, Compact neuromorphic system with four-terminal si-based synaptic devices for spiking neural networks. *IEEE Trans. Electron Devices* **64**, 2438–2444 (2017).
30. Y. Meng, C. Lan, F. Li, S. P. Yip, R. Wei, X. Kang, X. Bu, R. Dong, H. Zhang, J. C. Ho, Direct vapor-liquid-solid synthesis of all-inorganic perovskite nanowires for high-performance electronics and optoelectronics. *ACS Nano* **13**, 6060–6070 (2019).
31. S. Thiel, G. Hammerl, A. Schmehl, C. W. Schneider, J. Mannhart, Tunable quasi-two-dimensional electron gases in oxide heterostructures. *Science* **313**, 1942–1945 (2006).
32. L. Q. Zhu, C. J. Wan, L. Q. Guo, Y. Shi, Q. Wan, Artificial synapse network on inorganic proton conductor for neuromorphic systems. *Nat. Commun.* **5**, 3158 (2014).
33. Y. Wang, Z. Lv, J. Chen, Z. Wang, Y. Zhou, L. Zhou, X. Chen, S.-T. Han, Photonic synapses based on inorganic perovskite quantum dots for neuromorphic computing. *Adv. Mater.* **30**, 1802883 (2018).
34. B. Pradhan, S. Das, J. Li, F. Chowdhury, J. Cherusseri, D. Pandey, D. Dev, A. Krishnaprasad, E. Barrios, A. Towers, A. Gesquiere, L. Tetard, T. Roy, J. Thomas, Ultrasensitive and ultrathin phototransistors and photonic synapses using perovskite quantum dots grown from graphene lattice. *Sci. Adv.* **6**, eaay5225 (2020).
35. F.-S. Yang, M. Li, M.-P. Lee, I.-Y. Ho, J.-Y. Chen, H. Ling, Y. Li, J.-K. Chang, S.-H. Yang, Y.-M. Chang, K.-C. Lee, Y.-C. Chou, C.-H. Ho, W. Li, C.-H. Lien, Y.-F. Lin, Oxidation-boosted charge trapping in ultra-sensitive van der Waals materials for artificial synaptic features. *Nat. Commun.* **11**, 2972 (2020).
36. T. Chang, S.-H. Jo, W. Lu, Short-term memory to long-term memory transition in a nanoscale memristor. *ACS Nano* **5**, 7669–7676 (2011).
37. S. Gao, G. Liu, H. Yang, C. Hu, Q. Chen, G. Gong, W. Xue, X. Yi, J. Shang, R.-W. Li, An oxide Schottky junction artificial optoelectronic synapse. *ACS Nano* **13**, 2634–2642 (2019).
38. K. L. Magleby, The effect of repetitive stimulation on facilitation of transmitter release at the frog neuromuscular junction. *J. Physiol.* **234**, 327–352 (1973).
39. R. Shapley, M. Hawken, D. L. Ringach, Dynamics of orientation selectivity in the primary visual cortex and the importance of cortical inhibition. *Neuron* **38**, 689–699 (2003).
40. W. S. Geisler, D. G. Albrecht, Visual cortex neurons in monkeys and cats: Detection, discrimination, and identification. *Vis. Neurosci.* **14**, 897–919 (1997).
41. C. J. McAdams, J. H. R. Maunsell, Effects of attention on orientation-tuning functions of single neurons in macaque cortical area V4. *J. Neurosci.* **19**, 431–441 (1999).
42. S. Yu, B. Gao, Z. Fang, H. Yu, J. Kang, H.-S. P. Wong, A low energy oxide-based electronic synaptic device for neuromorphic visual systems with tolerance to device variation. *Adv. Mater.* **25**, 1774–1779 (2013).
43. C. J. Wan, L. Q. Zhu, Y. H. Liu, P. Feng, Z. P. Liu, H. L. Cao, P. Xiao, Y. Shi, Q. Wan, Proton-conducting graphene oxide-coupled neuron transistors for brain-inspired cognitive systems. *Adv. Mater.* **28**, 3557–3563 (2016).
44. Z. Wang, T. Zeng, Y. Ren, Y. Lin, H. Xu, X. Zhao, Y. Liu, D. Ielmini, Toward a generalized Bienenstock-Cooper-Munro rule for spatiotemporal learning via triplet-STDP in memristive devices. *Nat. Commun.* **11**, 1510 (2020).
45. F. Zhou, Z. Zhou, J. Chen, T. H. Choy, J. Wang, N. Zhang, Z. Lin, S. Yu, J. Kang, H.-S. P. Wong, Y. Chai, Optoelectronic resistive random access memory for neuromorphic vision sensors. *Nat. Nanotechnol.* **14**, 776–782 (2019).
46. S. Chen, Z. Lou, D. Chen, G. Shen, An artificial flexible visual memory system based on an UV-motivated Memristor. *Adv. Mater.* **30**, 1705400 (2018).
47. W. Kim, A. Javey, O. Vermesh, Q. Wang, Y. Li, H. Dai, Hysteresis caused by water molecules in carbon nanotube field-effect transistors. *Nano Lett.* **3**, 193–198 (2003).
48. J. K. Jeong, H. Won Yang, J. H. Jeong, Y.-G. Mo, H. D. Kim, Origin of threshold voltage instability in indium-gallium-zinc oxide thin film transistors. *Appl. Phys. Lett.* **93**, 123508 (2008).
49. J.-S. Park, J. K. Jeong, H.-J. Chung, Y.-G. Mo, H. D. Kim, Electronic transport properties of amorphous indium-gallium-zinc oxide semiconductor upon exposure to water. *Appl. Phys. Lett.* **92**, 072104 (2008).
50. P.-T. Liu, Y.-T. Chou, L.-F. Teng, Environment-dependent metastability of passivation-free indium zinc oxide thin film transistor after gate bias stress. *Appl. Phys. Lett.* **95**, 233504 (2009).
51. E. Di Gennaro, U. S. di Uccio, C. Aruta, C. Cantoni, A. Gadaleta, A. R. Lupini, D. Maccariello, D. Marré, I. Pallecchi, D. Paparo, P. Perna, M. Riaz, F. M. Granozio, Persistent photoconductivity in 2D electron gases at different oxide interfaces. *Adv. Opt. Mater.* **1**, 834–843 (2013).
52. Y. H. Liu, L. Q. Zhu, P. Feng, Y. Shi, Q. Wan, Freestanding artificial synapses based on laterally proton-coupled transistors on chitosan membranes. *Adv. Mater.* **27**, 5599–5604 (2015).
53. W. Xu, S.-Y. Min, H. Hwang, T.-W. Lee, Organic core-sheath nanowire artificial synapses with femtojoule energy consumption. *Sci. Adv.* **2**, e1501326 (2016).
54. P. Feng, W. W. Xu, Y. Yang, X. Wan, Y. Shi, Q. Wan, J. W. Zhao, Z. Cui, Printed neuromorphic devices based on printed carbon nanotube thin-film transistors. *Adv. Funct. Mater.* **27**, 1604447 (2017).
55. C. S. Yang, D. S. Shang, N. Liu, G. Shi, X. Shen, R. C. Yu, Y. Q. Li, Y. Sun, A synaptic transistor based on Quasi-2D molybdenum oxide. *Adv. Mater.* **29**, 1700906 (2017).
56. J.-T. Yang, C. Ge, J.-Y. Du, H.-Y. Huang, M. He, C. Wang, H.-B. Lu, G.-Z. Yang, K.-J. Jin, Artificial synapses emulated by an electrolyte-gated tungsten-oxide transistor. *Adv. Mater.* , 1801548 (2018).
57. W. Xu, T. L. Nguyen, Y.-T. Kim, C. Wolf, R. Pfattner, J. Lopez, B.-G. Chae, S.-I. Kim, M. Y. Lee, E.-Y. Shin, Y.-Y. Noh, J. H. Oh, H. Hwang, C.-G. Park, H. Y. Woo, T.-W. Lee, Ultrasensitive artificial synapse based on conjugated polyelectrolyte. *Nano Energy* **48**, 575–581 (2018).
58. J. Zhu, Y. Yang, R. Jia, Z. Liang, W. Zhu, Z. U. Rehman, L. Bao, X. Zhang, Y. Cai, L. Song, R. Huang, Ion gated synaptic transistors based on 2D van der waals crystals with tunable diffusive dynamics. *Adv. Mater.* **30**, 1800195 (2018).
59. L. Sun, Y. Zhang, G. Hwang, J. Jiang, D. Kim, Y. A. Eshete, R. Zhao, H. Yang, Synaptic computation enabled by joule heating of single-layered semiconductors for sound localization. *Nano Lett.* **18**, 3229–3234 (2018).
60. R. A. John, N. Tiwari, C. Yaoyi, Ankit, N. Tiwari, M. Kulkarni, A. Nirmal, A. C. Nguyen, A. Basu, N. Mathews, Ultralow power dual-gated subthreshold oxide neuristors: An enabler for higher order neuronal temporal correlations. *ACS Nano* **12**, 11263–11273 (2018).

61. R. A. John, F. Liu, N. A. Chien, M. R. Kulkarni, C. Zhu, Q. Fu, A. Basu, Z. Liu, N. Mathews, Synergistic gating of electro-iono-photoactive 2D chalcogenide neuristors: Coexistence of hebbian and homeostatic synaptic metaplasticity. *Adv. Mater.* **30**, 1800220 (2018).
62. D. Zheng, H. Fang, P. Wang, W. Luo, F. Gong, J. C. Ho, X. Chen, W. Lu, L. Liao, J. Wang, High-Performance ferroelectric polymer side-gated CdS nanowire ultraviolet photodetectors. *Adv. Funct. Mater.* **26**, 7690–7696 (2016).
63. X. Liu, L. Gu, Q. Zhang, J. Wu, Y. Long, Z. Fan, All-printable band-edge modulated ZnO nanowire photodetectors with ultra-high detectivity. *Nat. Commun.* **5**, 4007 (2014).
64. C.-H. Liu, Y.-C. Chang, T. B. Norris, Z. H. Zhong, Graphene photodetectors with ultra-broadband and high responsivity at room temperature. *Nat. Nanotechnol.* **9**, 273–278 (2014).
65. W.-Y. Kong, G.-A. Wu, K.-Y. Wang, T.-F. Zhang, Y.-F. Zou, D.-D. Wang, L.-B. Luo, Graphene-β-Ga_2O_3 heterojunction for highly sensitive deep UV photodetector application. *Adv. Mater.* **28**, 10725–10731 (2016).
66. D. Kufer, G. Konstantatos, Highly sensitive, encapsulated MoS_2 photodetector with gate controllable gain and speed. *Nano Lett.* **15**, 7307–7313 (2015).
67. N. Huo, G. Konstantatos, Ultrasensitive all-2D MoS_2 phototransistors enabled by an out-of-plane MoS_2 PN homojunction. *Nat. Commun.* **8**, 572 (2017).
68. F. Gong, W. Luo, J. Wang, P. Wang, H. Fang, D. Zheng, N. Guo, J. Wang, M. Luo, J. C. Ho, X. Chen, W. Lu, L. Liao, W. Hu, High-sensitivity floating-gate phototransistors based on WS_2 and MoS_2. *Adv. Funct. Mater.* **26**, 6084–6090 (2016).
69. C. Hu, D. Dong, X. Yang, K. Qiao, D. Yang, H. Deng, S. Yuan, J. Khan, Y. Lan, H. Song, J. Tang, Synergistic effect of hybrid PbS quantum Dots/2D-WSe_2 toward high performance and broadband phototransistors. *Adv. Funct. Mater.* **27**, 1603605 (2017).
70. X. Zhou, X. Hu, S. Zhou, H. Song, Q. Zhang, L. Pi, L. Li, H. Li, J. Lü, T. Zhai, Tunneling diode based on WSe_2/SnS_2 heterostructure incorporating high detectivity and responsivity. *Adv. Mater.* **30**, 1703286 (2018).
71. L. Li, W. Wang, Y. Chai, H. Li, M. Tian, T. Zhai, Few-Layered PtS_2 Phototransistor on h-BN with High Gain. *Adv. Funct. Mater.* **27**, 1701011 (2017).
72. T. Yang, Y. Zheng, Z. Du, W. Liu, Z. Yang, F. Gao, L. Wang, K.-C. Chou, X. Hou, W. Yang, Superior photodetectors based on all-inorganic perovskite $CsPbI_3$ nanorods with ultrafast response and high stability. *ACS Nano* **12**, 1611–1617 (2018).
73. B. Pradhan, G. S. Kumar, S. Sain, A. Dalui, U. K. Ghorai, S. K. Pradhan, S. Acharya, Size tunable cesium antimony chloride perovskite nanowires and nanorods. *Chem. Mater.* **30**, 2135–2142 (2018).
74. Q. Zhou, J. G. Park, R. Nie, A. K. Thokchom, D. Ha, J. Pan, S. I. Seok, T. Kim, Nanochannel-assisted perovskite nanowires: From growth mechanisms to photodetector applications. *ACS Nano* **12**, 8406–8414 (2018).
75. P. Gkoupidenis, N. Schaefer, B. Garlan, G. G. Malliaras, Neuromorphic functions in PEDOT:PSS organic electrochemical transistors. *Adv. Mater.* **27**, 7176–7180 (2015).
76. Y. Zang, H. Shen, D. Huang, C.-A. Di, D. Zhu, A dual-organic-transistor-based tactile-perception system with signal-processing functionality. *Adv. Mater.* **29**, 1606088 (2017).
77. R. A. John, J. Ko, M. R. Kulkarni, N. Tiwari, N. A. Chien, N. G. Ing, W. L. Leong, N. Mathews, Flexible ionic-electronic hybrid oxide synaptic TFTs with programmable dynamic plasticity for brain-inspired neuromorphic computing. *Small* **13**, 1701193 (2017).
78. L.-a. Kong, J. Sun, C. Qian, Y. Fu, J. X. Wang, J. L. Yang, Y. L. Gao, Long-term synaptic plasticity simulated in ionic liquid/polymer hybrid electrolyte gated organic transistors. *Org. Electron.* **47**, 126–132 (2017).
79. C. Wan, G. Chen, Y. Fu, M. Wang, N. Matsuhisa, S. Pan, L. Pan, H. Yang, Q. Wan, L. Zhu, X. Chen, An artificial sensory neuron with tactile perceptual learning. *Adv. Mater.* **30**, 1801291 (2018).
80. B. Li, Y. Liu, C. Wan, Z. Liu, M. Wang, D. Qi, J. Yu, P. Cai, M. Xiao, Y. Zeng, X. Chen, Mediating short-term plasticity in an artificial memristive synapse by the orientation of silica mesopores. *Adv. Mater.* **30**, 1706395 (2018).

Acknowledgments

Funding: We acknowledge the General Research Fund (CityU 11275916) and the Theme-based Research (T42-103/16-N) of the Research Grants Council of Hong Kong SAR, China, the National Natural Science Foundation of China (grant 51672229), the Science Technology and Innovation Committee of Shenzhen Municipality (grant JCYJ20170818095520778), and a grant from the Shenzhen Research Institute, City University of Hong Kong. **Author contributions:** Y.M., F.L., and J.C.H. conceived and designed the overall experiments. Y.M. and F.L. carried out experiments and collected related data. Y.M., F.L., R.W., X.B., T.T., and T.H. contributed to the analyses of the data. X.K., S.Y., C.L., F.W., and D.L. helped with electrical measurements. Y.M. and J.C.H. initiated the study. Y.M., K.N., T.Y., and J.C.H. wrote and revised the manuscript. All authors discussed the results and commented on the manuscript. **Competing interests:** The authors declare that they have no competing interests. **Data and materials availability:** All data needed to evaluate the conclusions in the paper are present in the paper and/or the Supplementary Materials. Additional data related to this paper may be requested from the authors.

Submitted 5 May 2020
Accepted 23 September 2020
Published 11 November 2020
10.1126/sciadv.abc6389

Citation: Y. Meng, F. Li, C. Lan, X. Bu, X. Kang, R. Wei, S. Yip, D. Li, F. Wang, T. Takahashi, T. Hosomi, K. Nagashima, T. Yanagida, J. C. Ho, Artificial visual systems enabled by quasi–two-dimensional electron gases in oxide superlattice nanowires. *Sci. Adv.* **6**, eabc6389 (2020).

Artificial visual systems enabled by quasi–two-dimensional electron gases in oxide superlattice nanowires

You Meng, Fangzhou Li, Changyong Lan, Xiuming Bu, Xiaolin Kang, Renjie Wei, SenPo Yip, Dapan Li, Fei Wang, Tsunaki Takahashi, Takuro Hosomi, Kazuki Nagashima, Takeshi Yanagida and Johnny C. Ho

Sci Adv **6** (46), eabc6389.
DOI: 10.1126/sciadv.abc6389